Coupling statistical indentation and microscopy to evaluate micromechanical properties of materials: Application to viscoelastic behavior of irradiated mortars

Benoit Hilloulin, Maxime Robira, Ahmed Loukili

Coupling statistical indentation and microscopy to evaluate micromechanical properties of materials: application to viscoelastic behavior of irradiated mortars

Benoit Hilloulin[a*], Maxime Robira[a,b,c], Ahmed Loukili[a]

[a] , *Institut de Recherche en Génie Civil et Mécanique (GeM), UMR-CNRS 6183, Ecole Centrale de Nantes, 1 rue de la Noë, 44321 Nantes, France – e-mail:* benoit.hilloulin@ec-nantes.fr; ahmed.loukili@ec-nantes.fr

[b] *SUBATECH, Unité Mixte de Recherche 6457, École des Mines de Nantes, CNRS/IN2P3, Université de Nantes, BP 20722, 44307 Nantes cedex 3, France – e-mail:* robira@subatech.in2p3.fr

[c] *Tractebel Engineering – Le Delage, 5 rue du 19 Mars 1962, 92622 Gennevilliers CEDEX, France*

[*] Corresponding author: Tel.: + 33 (0)2 40 37 16 61

Highlights

- Data mining principles applied to materials can lead to substantial improvements in the properties identification process.
- Coupling indentation and optical analysis reduces identified phase properties' variability.
- γ-irradiated mortar samples exhibit greater creep modulus and hardness and lower creep characteristic time than references.

Abstract

In this work, an original method coupling statistical indentation and 3D microscope image analysis for heterogenous materials characterization is developed. Statistical microindentation test results performed on γ-irradiated and pristine mortar specimens are presented and analyzed using a clustering data mining technique. The outputs are compared with the phase identification from 3D image analysis to effectively reduce uncertainties in the material properties of one of the phases (cement paste). With respect to the effects of irradiations on cementitious materials, a significant increase of cement paste creep modulus and hardness, and a significant decrease of creep characteristic time, are highlighted after an exposition of 257 kGy at 8.5 Gy /min. Young's modulus of the cement paste is not significantly affected. These results confirm macroscopic concrete creep observations presented in previous studies fitted with dose-dependent logarithmic laws.

Keywords: Indentation, Cement Paste (D), Mechanical properties (C), Creep (C), Radioactive Waste (E), Image analysis (B).

1. Introduction

The macroscopic mechanical properties of concrete mainly depend on micro-mechanical properties of its binding phase (i.e., the cement paste) and more particularly on the calcium silicate hydrate (CSH) gel, which exhibits significant local variations. For some years, microindentation and nanoindentation have been widely investigated to characterize elasto-plastic and creep properties of cementitious materials [1-4].

Indentation elastic parameters can then be input in homogenization schemes to determine concrete elastic properties [5-7].

According to Oliver and Pharr theory [8], the initial elastic unloading part of indentation curves can be analyzed to determine the indentation modulus and the indentation hardness of homogenous materials. Because cement paste is highly heterogenous, even at very small length scales, statistical nanoindentation performed at loads leading to penetration depths of some hundreds of nanometers has been developed. Assuming several phases may be indented at the same time, statistical indentation's main objective is to collect enough data points to apply a deconvolution algorithm giving the individual phase properties [9, 10]. However, two main critical aspects were identified regarding the application of statistical indentation technique to cementitious materials [11]: the size of the interaction volume may be larger than the size of the single phases at the risk of creating spurious peaks in the probability density function (PDF) [12, 13] as well as micromechanical values depending on the applied load [14], and the deconvolution analysis based on Gaussian Mixture itself may converge to local minima [15]. Therefore, coupling indentation results to other techniques identifying the effective nature of the indents is of great interest at different scales: using atomic force microscope [16] or SEM [6, 17, 18]. Coupling nanoindentation and SEM-EDS to filter data points, Chen et al. highlighted the presence of ultra-high density CSH/$Ca(OH)_2$ nanocomposites in low water-to-cement ratio cement paste by correlating micromechanical properties, e.g. indentation hardness or indentation modulus, to the portlandite volume fraction measured in volumes with approximately the same size as the one investigated through nanoindentation. Localization of indents by imaging techniques can also be used to differentiate the properties of several inclusions [19, 20] and eventually map a restricted area depending on the measured mechanical properties

[19, 21]. From the microscale to the macroscale, 3D image analysis of concrete or mortar surface appears to offer a promising field of research for purposes of generating geometric or topological data and supplementing other experimental techniques or providing input for numerical models [22-24].

Besides these developments concerning statistical indentation and imaging, it has been found out that the long-term creep properties of concrete specimens are related to the creep properties measured during minute-long microindentation or nanoindentation experiments. Both creep behaviors can be described using logarithmic time-dependent functions with two main variables: creep modulus and creep characteristic time [7, 25, 26]. Creep modulus of cement paste is linearly correlated with indentation hardness which means that the lower the hardness, the greater the creep strains, though the slope of the regression depends on the material: creep modulus of pure CSH is greater than the one of cement paste and it decreases with Ca/Si ratio [27]. Like macroscopic creep, indentation creep depends on the relative humidity [28].

In the context of nuclear waste disposals and, more generally, in the scope of nuclear safety structures characterization, the assessment of mechanical properties of irradiated concrete is of great interest to speculate over long term behavior of concrete under irradiations. Concrete properties evolutions with radiations have recently been summarized [29]. An extensive literature review ensures that irradiations lead to a decrease of the macroscopic strength of concrete under several types of radiations (α, γ and neutrons). The main mechanism behind concrete degradation under α-radiation is radiation-induced volumetric expansion (RIVE) of siliceous aggregates [30, 31] at doses greater than a reference dose of around 1×10^{20} n/cm^2 [32]. But under pure γ-radiation (exposition condition of structural concrete element of disposals [33]), degradation mechanisms are not understood yet and there is still a debate whether a reference level

of 2×10^5 kGy introduced some decades ago is relevant or not as some recent studies showed degradations after the exposure to lower doses [34, 35]. Water radiolysis triggered by γ-radiation is supposed to be the main phenomenon responsible of possible degradations located in the cement paste [36, 37] and phase alterations occurs only at very high doses of some dozens or even hundreds of MGy [38].Concrete creep under low dose irradiation (< 1 Gy / h [33]) is one of the major preoccupations concerning long-term behavior of waste disposal infrastructures. To our knowledge, only one study reported the smaller extent of creep of γ-irradiated concrete under compression, though measurements were carried out over a relatively short period of one year without any repetition [39].

The growing use of various data mining techniques in civil engineering and materials science applications is changing the way scientists and engineers are facing issues and creating promising paths of investigation at the same time. Larger datasets can be obtained and the challenge is to find useful and innovative information out of them [40]. Data mining techniques are being developed to identify materials properties [41] and even leading to the creation of novel materials. In civil engineering [42], data mining has mainly been used for large scale transportation problems for some years [43].

A main objective of the present work is to demonstrate the potential of data mining techniques for material properties identification in civil engineering at a microscale and mesoscale, at the crossroads of materials science and civil engineering. For this purpose, two complementary methods, namely statistical microindentation and microscopy, were performed on mortar specimens and combined to detect hidden data trends. Used together with adequate data mining techniques, microindentation data analysis and optical microscopy image analysis are shown to reduce the uncertainties associated with cement paste mechanical properties identification. An application to the determination

of mechanical properties of γ-irradiated mortars is then proposed. The first micro mechanical dataset of this type is reported and compared with the only, because tedious, measurement performed on concrete some decades ago [39]. Hundreds of measurement points obtained from 3 irradiated and 3 pristine control specimens are compared to highlight hidden trends due to radiation exposure.

2. Materials and methods

2.1 Specimens preparation and irradiation conditions

Mortar was prepared with CEM I 52.5 and 0/4 mm calcareous sand (to avoid the activation of alkali-silica reaction by irradiation) with the proportions detailed in Table 1. Any use of organic additives like superplasticizer or demolding oil was avoided to not induce a possible premature degradation by the irradiations. This mortar formulation was determined to be as representative as possible of a high-performance concrete used in nuclear waste storage facility galleries.

Six mortar prisms with dimensions of 4 x 4 x 16 cm^3 were cast in polypropylene molds to avoid any presence of metallic compounds from the molds. After 1 day of curing under sealed conditions in an air-conditioned room at a temperature of 20°C and 90% RH, the specimens were demolded. The specimens were further cured in lime-saturated water until the age of 28 days. Mortar prisms were then dried during 14 days in an oven at 45°C (a constant mass was measured at 10 days).

Half of the mortar prisms (MD-257kGy-I1 to MD-257kGy-I3) were then introduced in an irradiator at ARRONAX (^{137}Cs source, 661 keV, 123.4 TBq) at the age of 42 days. Specimens were exposed as close to the source as possible to guarantee a spatially homogenous dosage during 3 weeks. The total γ dose received by the specimens was calculated to be around 257 kGy based on a map of the γ fluxes in the irradiator realized

by Fricke dosimetry measurement. The other half of the specimens (MD-257kGy-S1 to MD-257kGy-S3), e.g. the control specimens, were kept in an air-conditioned room at relative humidity of around 65% close to the ones measured in the irradiator at the end of the irradiation period.

Table 1. Mortar compositions

Cement (kg/m^3)	Calcareous Sand 0/4 (kg/m^3)	Water (kg/m^3)	W/C	Paste volume (%)
566	1344	270	0.43	45

Several mechanical and chemo-physical tests were performed on these mortars and on other series as well. The results will be presented in future communications but, in the sake of clarity, some results may be evocated in regards to micromechanical results presented herein. No evident carbonation, pore size evolution or hydrated phases transformations were measured. Thus micromechanical properties evolutions may not be attributed to calcite formation in contrast with [44].

2.2 Indentation setup and theory

Microindentation tests were performed during the week following the irradiation period with the main objective of comparing the properties of irradiated and control specimens. Thus, a volume of 2 x 2 x 1.5 cm^3 was sawn from the middle part of a half of the 4 x 4 x 16 cm^3 broken by three-point bending test. This location was selected to avoid damage due to the three-point bending test. The 2 x 2 cm^2 section was polished with Si-C paper with decreasing particle size (500, 1200, 2000, 4000) using ethanol as polishing liquid. Polishing times were selected around some minutes per paper to limit the risk of aggregate cracking. These times are much shorter than the ones used for

171 nanoindentation on cement pastes [45] but were sufficient to obtain a surface roughness
172 R_q of around 0.5 - 1 µm which is acceptable for micro-indentation with penetration
173 depth of some microns.
174 A typical cement paste area with a typical indent is presented in Fig. 1. As it can be
175 observed, the scale of the indent is larger than the characteristic scale of the
176 microstructure of the cement paste (residual anhydrous clinker size): thus, the
177 performed microindentation tests provided the mechanical properties of the cement
178 paste or the sand, or the interface and not of the individual phases of the cement paste.
179 Microindentation was performed using a Vickers indenter probe over a grid of
180 20 x 20 points, evenly spaced by 500 µm to investigate a representative surface of
181 1 x 1 cm² of the mortar sample. For each indent, the load was increased linearly over
182 time in 5 s up to 2000 mN, kept constant during the 60 s holding phase, and decreased
183 linearly over time back to zero in 5 s. The very short loading time was selected to limit
184 creep during this period and do not apparently damaged the sample.

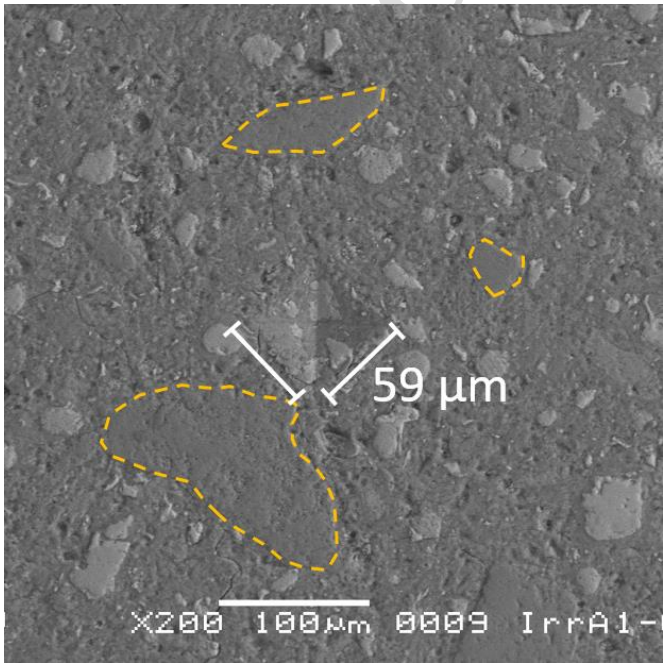

Fig. 1. SEM observation of a typical indent located in the cement paste with a width of 59 µm (small sand fines located near the indent are circled by orange dashed lines).

Various properties were calculated from the load – penetration curves. First, the indentation hardness depending on the maximum load and the projected contact area:

$$H_{IT} = \frac{P_{max}}{A_p(h_c)} \quad (1)$$

For Vickers' indenter the projected contact area can be estimated by:

$$A_p(h_c) = 24.50 h_c^2 \quad (2)$$

Where h_c can be calculated based on maximum indentation depth h_{max} assuming:

$$h_c = h_{max} - \varepsilon(h_{max} - h_r) \quad (3)$$

with $\varepsilon = 0.75$ and h_r is the final ideal penetration height can be determined. Martens hardness was also computed according to:

$$H_M = \frac{P_{max}}{A_s(h)} \quad (4)$$

Where $A_s(h)$ is the contact area, depending on the indentation depth *h*, defined for a Vickers indenter by:

$$A_s(h) = \frac{4\sin(\alpha/2)}{\cos^2(\alpha/2)} h^2 \approx 26.43 h^2 \quad (5)$$

With α=136° the top angle of the Vickers pyramid.

The Young's modulus E_{IT} of the indented material is given by:

$$M = \frac{E_{IT}}{1 - \nu_s^2} = \frac{1}{\frac{1}{E_r} - \frac{1}{M_{ind}}} \quad (6)$$

Where M denotes the indentation modulus, M_{ind} = 1140 GPa the modulus of the indenter, ν_s the Poisson ratio of the material (considered equal to 0.2, a possible

200 variation of some percent of EIT may be induced for other values of Poisson ratio) and
201 E_r is the reduced modulus which is determined assuming:

$$E_r = \frac{1}{2}\left(\frac{dP}{dh}\sqrt{\frac{\pi}{A}}\right) \text{ at } h = h_{max} \quad (7)$$

202 A first creep parameter C_{IT}, e.g. the normalized indentation creep parameter, was
203 calculated by the machine. It is defined as:

$$C_{IT}(\%) = \frac{h_{max} - h_1}{h_1} \times 100 \quad (8)$$

204 With h_1 the indentation depth at the beginning of the creep stage.
205 Energetic parameters n_{IT} and W_t were also recorded. n_{IT} is the proportion of the elastic
206 response relatively to the total energy W_t: $n_{IT} = W_{elas} / W_t$.
207 More meaningful creep parameters C and τ can be extracted from the indentation curves
208 (see Fig 2a)) calculating the creep function $L(t)$ [21]:

$$L(t) - L(0) = L(t) - \frac{1}{M} = \frac{2a_u \Delta h(t)}{P_{max}} \quad (9)$$

209 Where $\Delta h(t)$ denotes the indentation depth increase during the constant load phase, a_u
210 denotes the is the radius of the equivalent projected contact area between the indenter
211 probe and the indented surface at the onset of unloading
212 Assuming a logarithmic fit of the creep function, the creep parameters are defined
213 according to [25]:

$$L(t) - \frac{1}{M} = \frac{\ln(t/\tau + 1)}{C} \quad (10)$$

214 It was verified that this law can adequately reproduce the creep behavior of both cement
215 paste and sand as illustrated in Fig. 2 b). In order to avoid drying during creep
216 experiments, indentation was realized at a relative humidity close to the one imposed
217 during the irradiation period (around 65% RH). Moreover, autogenous shrinkage of the

218 sample can be neglected at the age of 72 d. Then, the creep function is expected to
219 characterize the basic creep behavior of the specimens.
220

a)

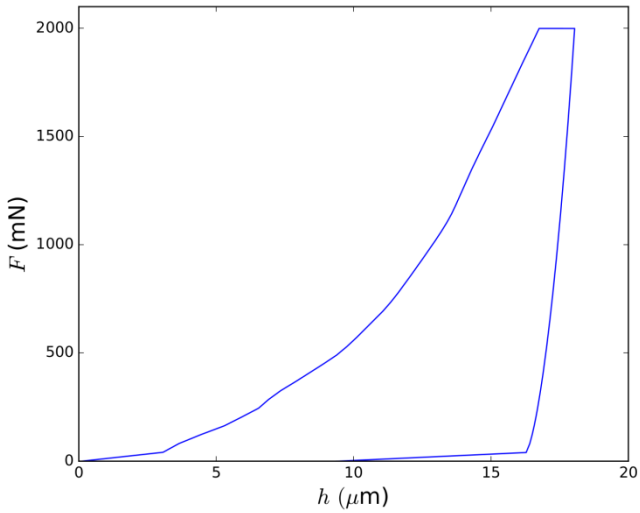

b)

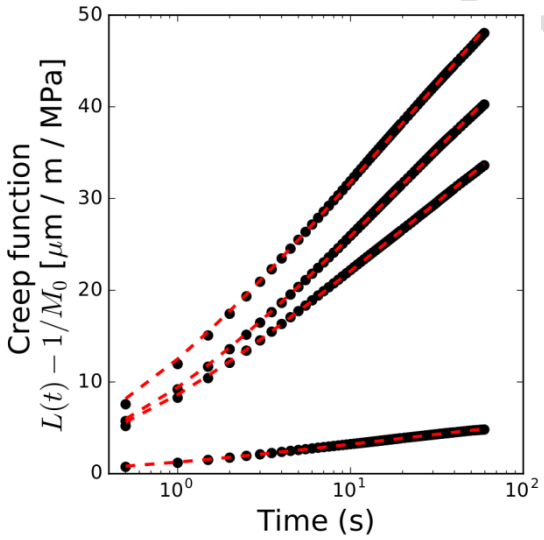

221 **Fig. 2.** Microindentation outputs: a) raw load – penetration curve, b) fitting the creep
222 function by a logarithmic law (3 curves correspond to cement paste indents and 1 to a
223 sand indent)
224

2.3 3D microscope measurements and analysis

After indentation, a map of the indented zone was realized using a Hirox RH-2000 3D microscope by merging around 200 3D reconstructed images evenly spaced along the indented area. The selected magnification (x 140) led to a final horizontal resolution of the 2D projected image of 1.5 µm / pix which is adequate to correctly locate the indents and assess their nature. Because some indents may be hardly located, especially the ones created in voids, a basic routine was implemented in Python to locate all the indents based on the location of 3 of them by drawing blue squares on the original image. As illustrated in Fig. 3, the 20 x 20 matrix of indents covers a sufficiently large area representative of the mortar volume and the reconstructed image correctly represent the matrix without image distortion due to multiple image merging (it was verified that the indents were correctly located by the blue squares). The nature of the indents was then manually identified because color-based filters were found to be relatively imprecise in the case of such mortar images.

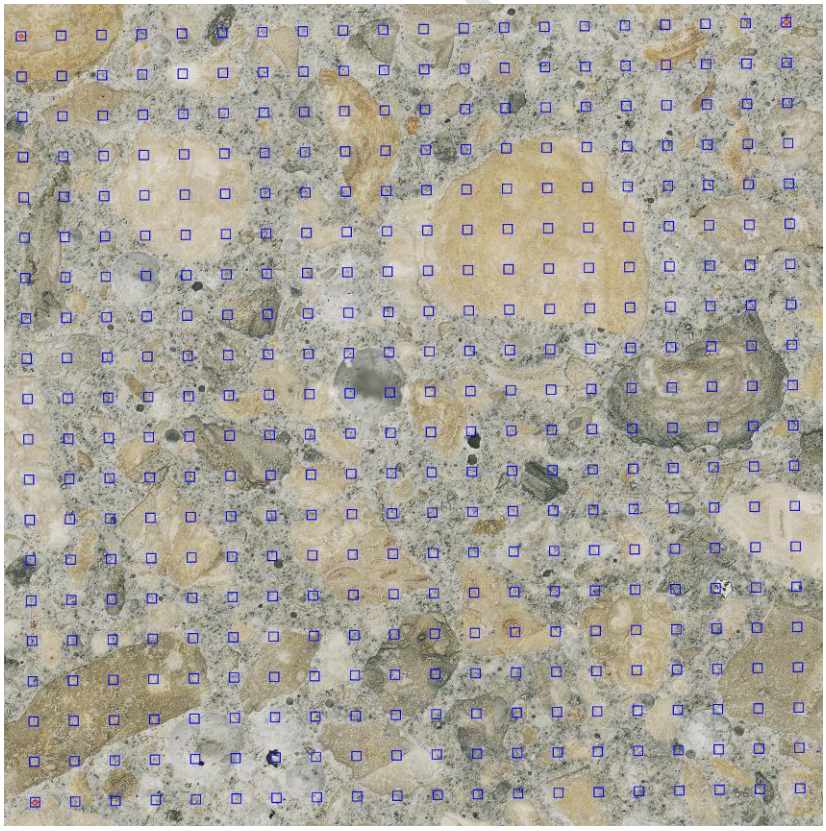

Fig. 3. 2D projected global view of the 20 x 20 matrix of indents over a 1 x 1 cm² surface from 3D microscope acquisition (indents are indicated by blue squares)

3. Results and discussion

3.1 Statistical indentation data deconvolution and its variability

First, indentation outputs from each specimen were visualized by mean of a scatter plot as illustrated in Fig. 4. Several basic observations directly arise from the analysis of the scatter plot. Some data points are isolated from the others. These isolated points are mainly indents with a maximum penetration depth h_{max} greater than 20 µm. In order to properly run data deconvolution, these points were filtered out on all samples. As we will see in the next paragraph, they correspond to indents close to voids or local defects and therefore do not correctly represent cement paste properties. Due to sand heterogeneities, some data points exhibit indentation hardness greater than 2500 MPa. Such points were also filtered out of the analysis. Already reported correlations can be highlighted in the scatter plot: correlation between hardness and Young's modulus, linear-shaped correlation between hardness and creep modulus. Looking at the PDFs located along the diagonal of the scatter plots, one may also observe that two main groups, presumably the cement paste and the sand, can be identified (especially on H_{IT} and E_{IT} PDFs). However, these two groups considerably overlap each over, probably due to a non-negligible proportion of the indents at the interface between cement paste and sand grains.

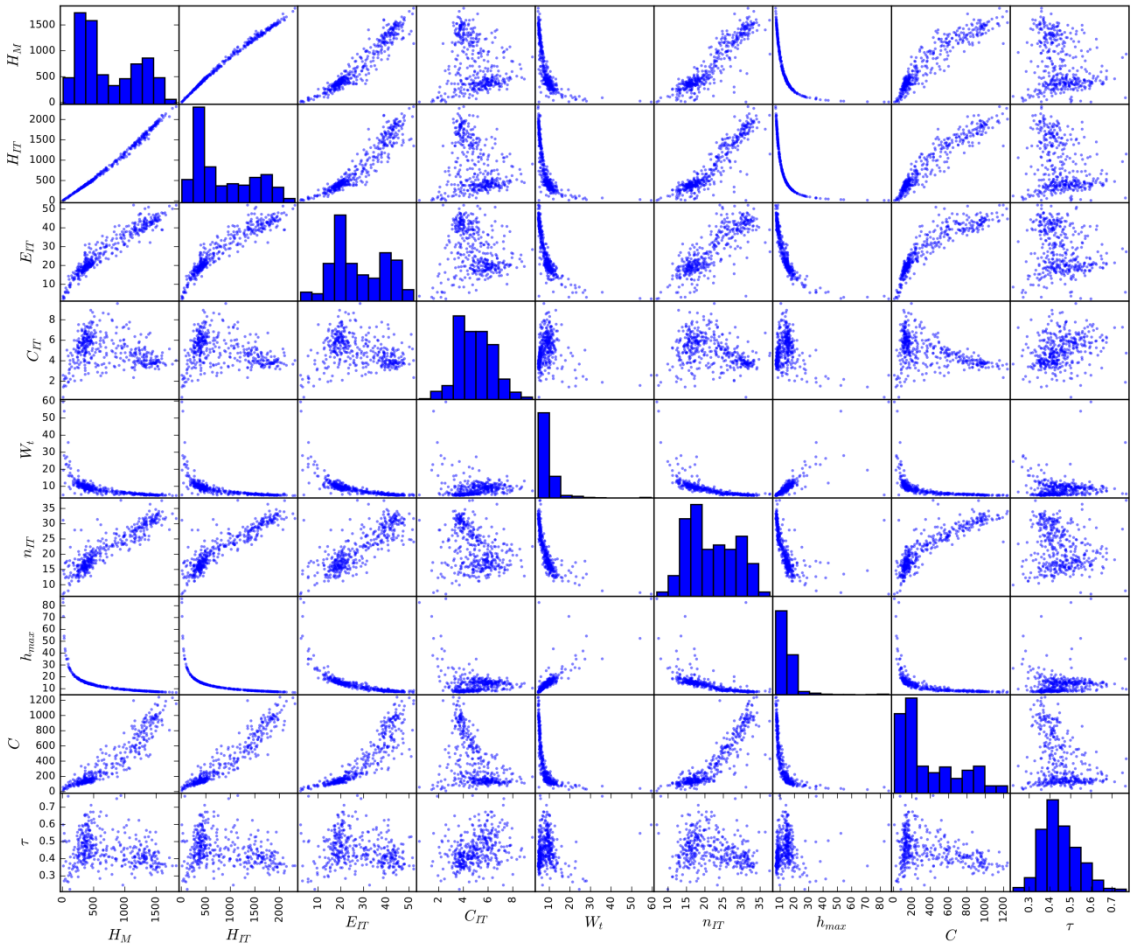

Fig. 4. Unfiltered scatter plot from sample MD-257kGy-S3 (H_M and H_{IT} are expressed in MPa, E_{IT} and C in GPa, C_{IT} and n_{IT} in %, W_t in µJ, h_{max} in µm and τ in s).

Then, data points repartition was visualized using a Euclidian distance-based dendrogram generated from the 9 output variables as illustrated in Fig 5 a). This way, the similarities between the data points can be highlighted without subjectivity (subjectivity may come from the arbitrary choice of the number of clusters prior to deconvolution, the output variables used to generate the clusters, e.g. typically 2 [9] or 3 [14] only). The data points mainly belong to two dissimilar groups joining at a high around 60 and with their subgroups differentiated at highs around 20.

Cutting the dendrogram at a high of 30 leads to a 2-groups hierarchical clustering represented on a C-H_{IT} 2D plane (Fig. 5 b)) with one group probably mainly composed of cement paste and one group probably mainly composed of sand. Cutting the

dendrogram at a high of 20 leads to 3 groups (Fig. 5 c)). Naturally, because of hierarchical clustering principles, only one of the two groups has been divided into two subgroups, and for most of the mortar samples it is the group with the highest hardness (presumably sand indents). Then, it means that, at the selected indentation load, sand grains are more heterogeneous than the cement paste. It also leads to another observation: 2-groups (and 3-groups) hierarchical clustering clearly overestimates cement paste proportion, if one basically assumes that the group with the smallest mean hardness corresponds to the cement paste. Indeed, reading the dendrogram, the horizontal proportion of the first group corresponding to the lowest hardness is greater than the one of the second group corresponding to the highest hardness. As the horizontal axis is composed of all the single data points, it would mean that the number of indents in the cement paste is greater than the number of indents in the sand. That is a biased conclusion because the paste volume fraction is only of 45% (and at this indentation load, an important number of indents are located at the interface between cement paste and sand grains and they would lead to intermediate properties). This erroneous prediction of the phase volume fractions has already been reported elsewhere and the assignation of mean phases properties based on numerical data deconvolution is questionable [15]. This basic observation motivates the use of optical techniques described hereafter to filter experimental data based on indents nature.

Reporting the nature of the indents predicted by deconvolution over the microscopic image as illustrated in Fig. 6, a relatively good correspondence is noticeable: red squares corresponding to the first deconvoluted group are mainly located in the paste and blue ones, corresponding to the second group are mainly located in sand grains, while black squares, corresponding to initially filtered values are all near voids. However, some indents (2 of them were circled in orange as examples) numerically

identified as cement paste are located on sand grains and vice versa which emphasizes the limits of numerical clustering.

a)

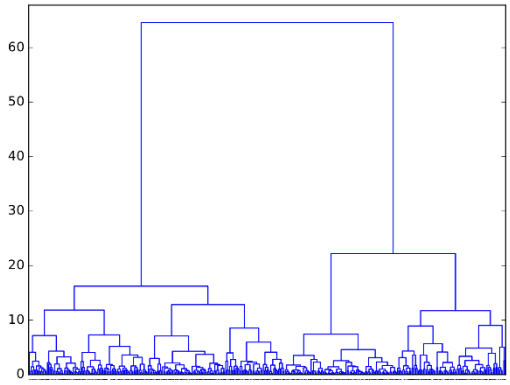

b)

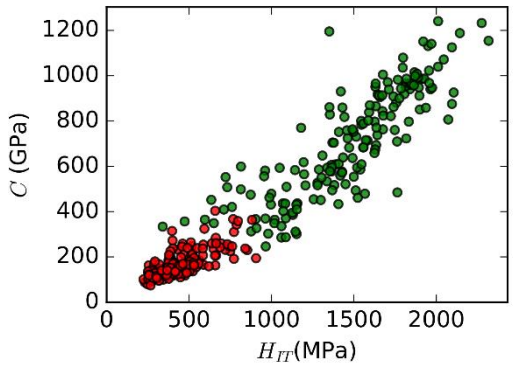

c)

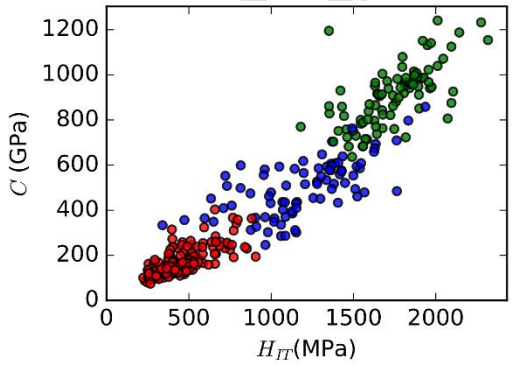

Fig. 5. Hierarchical clustering strategy applied to specimen MD-257kGy-S3: a) Euclidian distance-based dendrogram (with the 400 individual data points on the x-axis), b) and c), data points repartition along C-H_{IT} plane using a 2-groups separation (b) and a 3-groups separation (c).

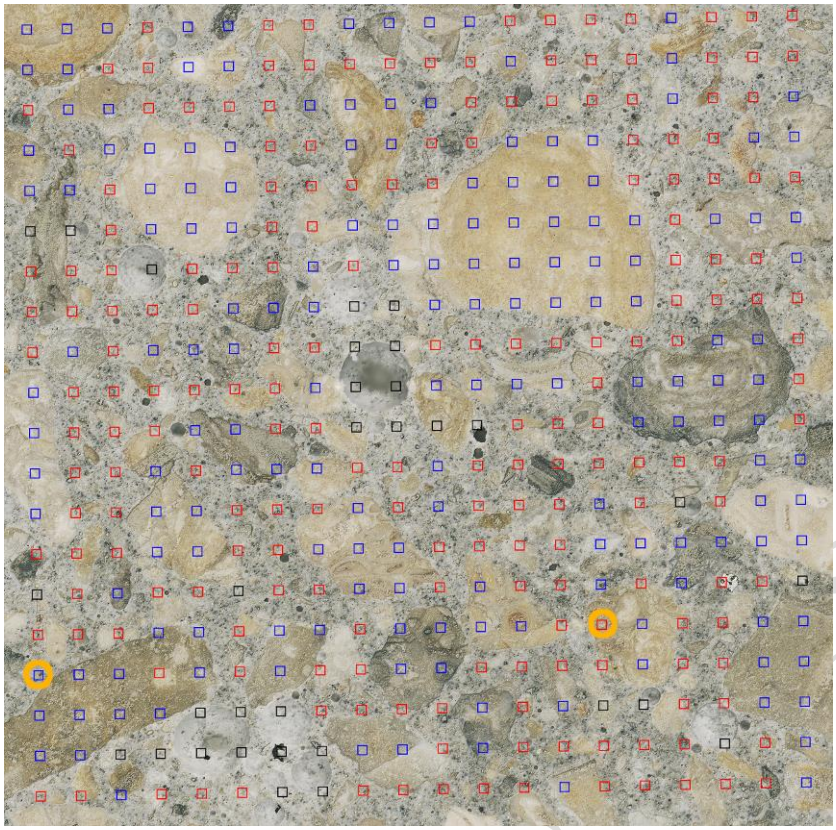

Fig. 6. Representation on the 3D microscopic image of specimen MD-257kGy-S3 of the nature of the indents predicted by data deconvolution (red squares correspond to group 1, e.g. 'paste', blue squares to group 2, e.g. 'sand, and black squares to filtered values before the analysis). Orange circles indicate two indents attributed to the wrong group as an example of the limits of numerical clustering. Indentation area extends over $1 \times 1 cm^2$.

3.2 3D microscope results

Indents were visually classified into 4 groups: voids, paste, sand and interface between paste and sand so that the latter 3 could be compared to the 3 groups obtained by hierarchical clustering. As illustrated in Fig. 7, there is an important proportion of indents located at the cement paste - sand grains interface marked by green squares. This is directly correlated to the indent size relatively to the size of the phase and the

volume fraction of sand. Comparing Fig. 6 with Fig. 7, one may notes that the other indents are on majority of the same nature as the indents attributed to one group using the hierarchical clustering method.

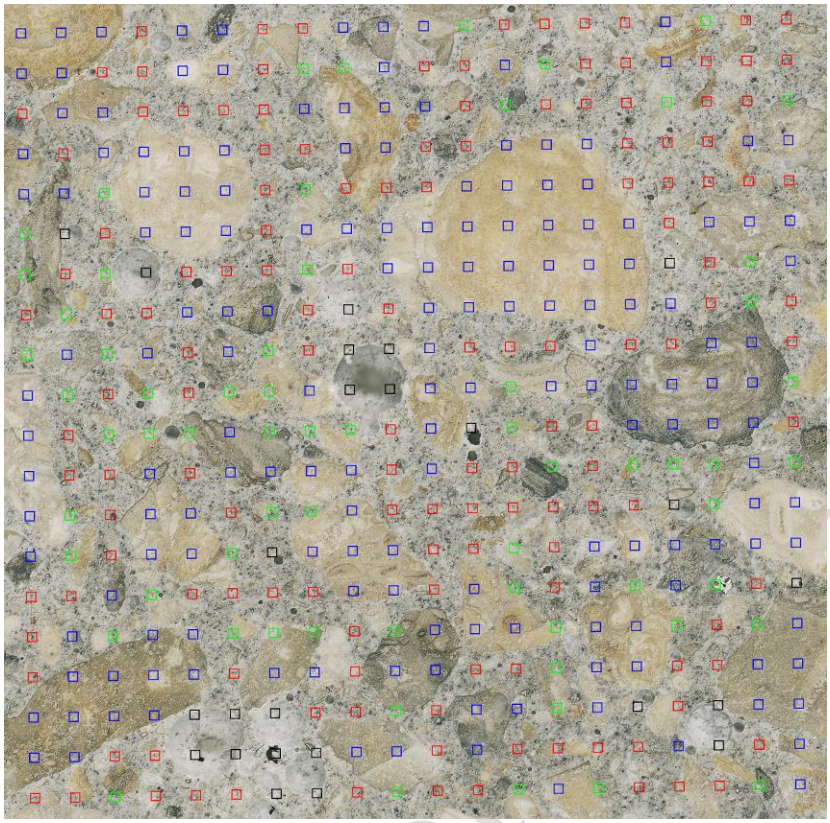

Fig. 7. Indents location and nature of specimen MD-257kGy-S3 (paste in red, cement paste - sand grain interface in green, pure sand in blue, void in black) according the 3D microscope image analysis.

From the repartition of the indented outputs variables per groups using 3D microscope (Fig. 8), it can be observed that cement paste and sand indentation variables distributions closely match normal distributions. On the other side, properties associated with indents located at interfaces between cement paste and sand grains (green histograms) are much more variables and do not follow any specific distribution. This is due to the fact that indents on interfaces could either exhibit the mean value when two phases properties are probed (for example there are a lot of indents on interfaces with

335 Young's modulus between 25 and 35 GPa, because this property is representative of a
336 large volume), either be very similar to cement paste or sand properties because the
337 indenter probe slide to one side during loading (most of the time, to the cement paste
338 side because of its lower altitude). For this reason, a lot of indents on interfaces have an
339 indentation hardness around 500 MPa, e.g. around the mean value of indents attributed
340 to the cement paste as this property is representative of a smaller volume.
341 Identifying phases properties based on imaging is therefore possible for predominant
342 phases like cement paste or sand. Distributions are well defined but some indents
343 properties are possibly associated with the wrong group. For example, in Fig. 8, one can
344 see that some indents with high hardness and creep modulus (around 1 GPa and
345 400 GPa resp.) were identified as cement paste while some indents with Young's
346 modulus lower than 15 GPa were identified as sand grains. More than half of these
347 values are associated with either an odd indent shape on sand or the presence of very
348 small sand grains close to an indent attributed to the cement paste (most of these indents
349 are probably rightly on cement paste but the indentation variables may be influence by
350 very close sand grains even under the indent). Thus, although the optical identification
351 of the indents should be attractive and sufficient in some cases, the combination of a
352 numerical deconvolution technique and of an imaging technique may help reduce the
353 uncertainties concerning some minor odd indents outputs.

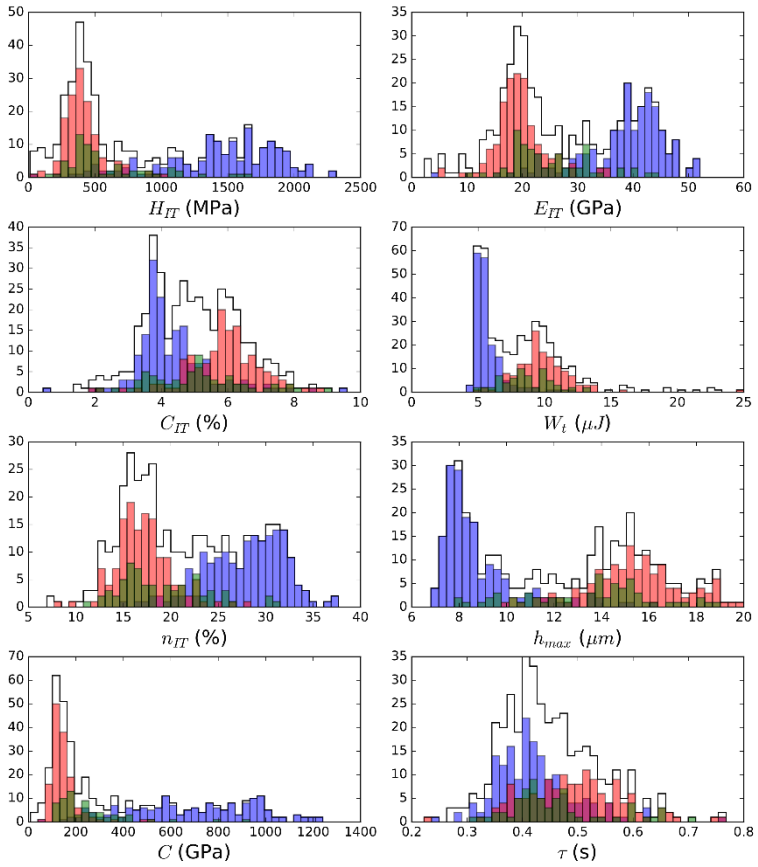

Fig. 8. Histograms of distributions of the indentation output variables of specimen MD-257kGy-S3. Total distribution is represented by the continuous black line, distributions of the phases identified using the 3D microscope are colored in red (cement paste), blue (sand grains) and green (cement paste – sand grain interface).

3.3 Combination of 3D microscope and indentation results

3D microscope and indentation data deconvolution phase assignations were combined to reduce the variability of the identified phase properties. Comparing the indent natures from the two first order techniques (3D microscope 3 groups identification vs 3 groups hierarchical clustering), the indents with corresponding natures were considered as representative of a given phase while the others were considered as non-reliable information regarding the final application of this study, e.g. cement paste characterization. This coupling may address the two main preoccupations of the first

order analysis: concerning numerical clustering this method can effectively provide a supplementary information about the nature of the indents and, concerning optical clustering, the method can considerably decrease the risk of false identification (either due to the operator or to the image precision) by selecting clusters of indents with close micromechanical properties.

From a visual inspection of the spatial repartition of the nature of the indents in one of the worst cases (Fig. 9), it should be observed that there is a huge proportion of noncorresponding indent natures (yellow squares). Indeed, when comparing 3 groups from 3D microscope identification and 3 groups from data deconvolution, around 35% of indents nature do not correspond between the two analysis, while this proportion is usually around 25% for the comparison between 3 groups from 3D microscope and 2 groups from data deconvolution. A majority of noncorresponding indents are located in sand grains or at their periphery and this is the reason explaining why there is less error using 2 groups data from deconvolution data: data points numerically identified as belonging to the intermediate group were mostly visually identified as sand grains and not sand grain – cement paste interface. Only a very few indents were identified as interfaces by combining the two methods which means that groups identified by clustering algorithms with intermediate properties are not necessarily different phases (here sand grain – cement paste interface). Moreover, the variability of sand grain properties could also be visualized as for some sand grains almost all indents are corresponding ones, while for others, probably with smaller hardness, indents are mostly noncorresponding ones (identified as sand for one analysis, interface for the other).

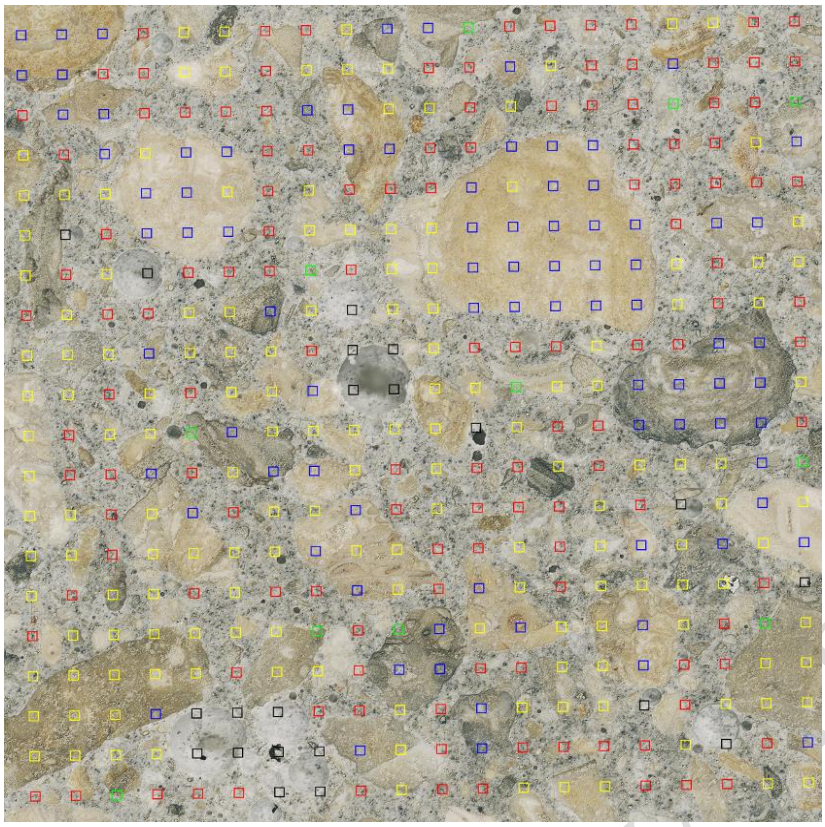

Fig. 9. Indents location and nature of specimen MD-257kGy-S3 comparing 3D microscope image analysis and 3 groups hierarchical data deconvolution (paste in red, cement paste - sand grain interface in green, pure sand in blue, void in black and indents with noncorresponding natures between the two analyses in yellow).

A detailed analysis of the microindentation output variables through histograms (Fig. 10) reveals that noncorresponding indents are mainly the ones with intermediate properties as predicted by the visual observation. Interestingly, the initial goal of this comparison method seems to have been achieved: cement paste and sand distributions are tightened and do not overlap for Young's modulus, hardness and creep modulus. Moreover, some of the extreme values are filtered out. Thus, the comparison of numerical data deconvolution and optical data clustering efficiently reduces the uncertainties concerning phase identification because of the complementarity between the two methods.

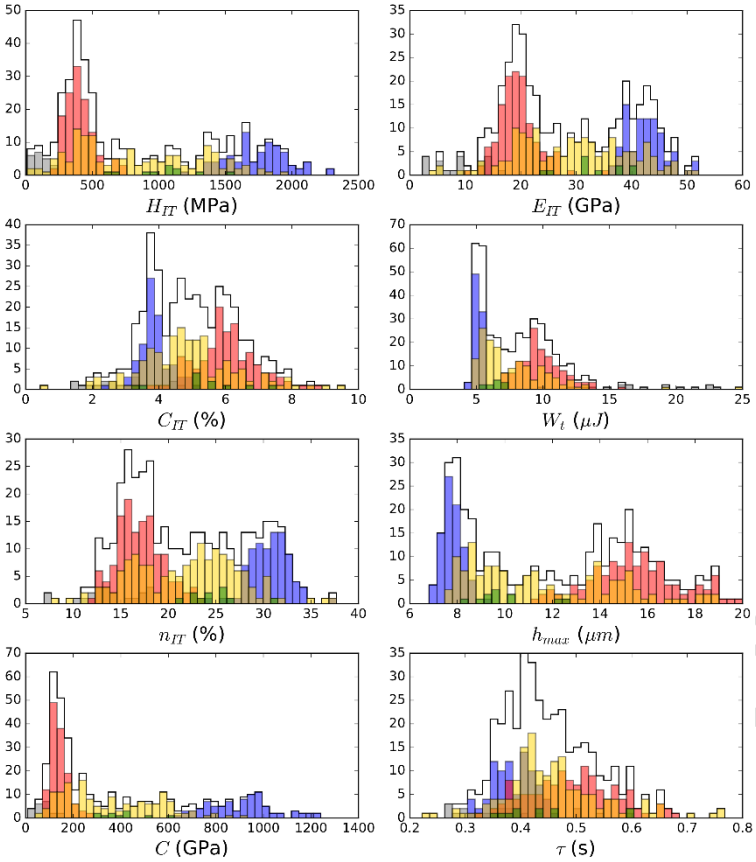

Fig. 10. Histograms of distributions of the indentation output variables of specimen MD-257kGy-S3 after the combined use of numerical and clustering and image analysis. Total distribution is represented by the continuous black line, distributions of the phases are colored in red (cement paste), blue (sand grains), green (sand grain – cement pastes interface). The distribution of noncorresponding indents is represented in yellow.

3.4 Creep properties of γ-irradiated mortar specimens

Using the method described in the previous paragraphs, cement paste properties of irradiated and control mortar specimens were compared. Tables 2 to 4 summarize the indentation outputs associated with hierarchical clustering, 3D-microscope image analysis and the method coupling numerical indentation data clustering and 3D-microscope image analysis. As explained, the main interest of the technique is to reduce

the variability of the indentation outputs attributed to one phase, here the cement paste. This objective is achieved for most of the outputs as the variances of the outputs variables distributions in Table 4 are smaller than the corresponding ones on Table 2 and 3 both on individual specimens and on the two series merging data from the 3 specimens per series. Moreover, mean values of hardness, Young's modulus, creep parameter are smaller on Table 4 because some data points with intermediate properties were filtered out comparing numerical clustering and optical clustering.

One may finally observe that it is rather difficult to draw some conclusions on the evolution of the output variables due to irradiations from these data as the standard error (square-root of the variance) is close or greater than the difference between the two series. Thus, indentation outputs were grouped together whether they belong to irradiated specimens or not. The merged data is represented on Fig. 11. Analyzing non-diagonal graphics, one may observe that data points are rather well concentrated and dispersion limited. On diagonal probability distributions (PDF), a clear shift of C due to irradiations can be observed towards greater values while τ decreases. Indentation hardness also seems to be affected, though statistical analysis is necessary to conclude concerning a possible influence of irradiations.

438 **Table 2.** Indentation outputs for cement paste indents identified using hierarchical

439 clustering (means and variances in brackets).

	HM (MPa)	HIT (MPa)	EIT (GPa)	CIT (%)	Wt (µJ)	nIT (%)	hmax (µm)	C (GPa)	τ (s)
MD-257kGy-I1	377.4	402.7	19.5	5.16	10.2	16.7	15.40	173	0.384
	(5424)	(6192)	(5.2)	(1.22)	(2.0)	(4.2)	(2.30)	(1111)	(0.005)
MD-257kGy-I2	432.0	466.6	21.0	5.20	9.3	18.1	14.54	197	0.416
	(13035)	(16610)	(15.5)	(1.51)	(2.8)	(8.1)	(3.30)	(3534)	(0.007)
MD-257kGy-I3	438.8	478.8	21.3	5.04	9.2	19.0	14.46	210	0.447
	(16321)	(22917)	(28.2)	(1.02)	(2.8)	(14.9)	(3.92)	(8623)	(0.005)
MD-257kGy-S1	396.9	415.4	20.2	6.00	10.1	16.7	15.26	149	0.465
	(9088)	(10205)	(8.4)	(1.29)	(2.4)	(6.2)	(3.13)	(1006)	(0.005)
MD-257kGy-S2	369.3	395.2	19.9	4.99	9.7	17.5	15.58	182	0.426
	(6869)	(8737)	(12.5)	(1.89)	(3.0)	(10.5)	(2.79)	(4653)	(0.006)
MD-257kGy-S3	416.1	441.0	20.8	5.77	9.7	17.3	15.01	165	0.481
	(16467)	(20063)	(18.1)	(1.43)	(3.2)	(7.4)	(4.34)	(3481)	(0.007)
MD-257kGy-I	421.8	456.2	20.7	5.13	9.5	18.1	14.71	196	0.420
	(13019)	(17314)	(18.2)	(1.27)	(2.7)	(10.4)	(3.43)	(4998)	(0.006)
MD-257kGy-S	396.2	420.2	20.4	5.55	9.8	17.2	15.25	168	0.459
	(12102)	(14600)	(14.4)	(1.73)	(3.0)	(8.3)	(3.62)	(3539)	(0.007)

440

441 **Table 3.** Indentation outputs for cement paste indents identified using 3D-microscope

442 image analysis (means and variances in brackets).

	HM (MPa)	HIT (MPa)	EIT (GPa)	CIT (%)	Wt (µJ)	nIT (%)	hmax (µm)	C (GPa)	τ (s)
MD-257kGy-I1	440.8	476.8	21.2	5.24	9.4	18.0	14.50	199	0.400
	(19742)	(27060)	(12.9)	(1.29)	(2.9)	(11.9)	(3.92)	(4667)	(0.005)
MD-257kGy-I2	434.1	468.9	20.6	5.33	9.4	17.9	14.60	192	0.425
	(17383)	(23191)	(16.4)	(1.20)	(3.0)	(8.3)	(3.82)	(4943)	(0.007)
MD-257kGy-I3	431.9	464.6	20.4	5.63	9.3	18.6	14.64	177	0.478
	(15769)	(21090)	(20.5)	(1.15)	(2.2)	(12.4)	(3.50)	(4922)	(0.007)
MD-257kGy-S1	480.2	509.0	22.4	6.39	9.1	18.1	14.01	166	0.558
	(22752)	(32818)	(15.9)	(0.97)	(2.3)	(10.6)	(3.09)	(5071)	(0.013)
MD-257kGy-S2	412.5	443.9	20.3	5.44	9.6	17.6	15.17	180	0.435
	(28845)	(42071)	(18.6)	(1.62)	(2.8)	(9.7)	(4.73)	(8569)	(0.005)
MD-257kGy-S3	402.8	425.0	20.0	6.00	9.7	17.3	15.29	151	0.495
	(16326)	(20613)	(18.6)	(0.96)	(3.2)	(8.1)	(4.33)	(3661)	(0.007)
MD-257kGy-I	435.7	470.2	20.8	5.40	9.4	18.2	14.58	190	0.434
	(17592)	(23734)	(16.5)	(1.24)	(2.7)	(10.9)	(3.74)	(4898)	(0.007)
MD-257kGy-S	432.2	459.5	20.9	5.95	9.5	17.7	14.82	165	0.497
	(23588)	(32752)	(18.8)	(1.32)	(2.8)	(9.6)	(4.36)	(5814)	(0.011)

443

Table 4. Indentation outputs for cement paste indents identified using the proposed method coupling numerical clustering and image analysis (means and variances in brackets).

	HM (MPa)	HIT (MPa)	EIT (GPa)	CIT (%)	Wt (µJ)	nIT (%)	hmax (µm)	C (GPa)	τ (s)
MD-257kGy-I1	376.0 (5267)	400.6 (5997)	19.4 (4.8)	5.25 (1.21)	10.2 (2.1)	16.6 (4.6)	15.44 (2.26)	168 (919)	0.391 (0.004)
MD-257kGy-I2	416.9 (11407)	448.1 (14084)	20.2 (12.8)	5.33 (1.22)	9.6 (2.8)	17.6 (6.6)	14.79 (3.20)	183 (2896)	0.429 (0.007)
MD-257kGy-I3	397.8 (8279)	428.1 (11073)	19.7 (19.3)	5.35 (0.91)	9.6 (2.1)	18.1 (12.2)	15.09 (2.79)	174 (4012)	0.454 (0.004)
MD-257kGy-S1	411.2 (8037)	428.4 (9145)	20.4 (7.9)	6.33 (0.77)	10.2 (2.4)	16.4 (4.8)	15.00 (2.59)	144 (773)	0.476 (0.004)
MD-257kGy-S2	372.3 (9381)	395.0 (11590)	19.6 (13.0)	5.40 (1.63)	9.9 (2.5)	16.9 (5.5)	15.63 (2.92)	162 (2310)	0.439 (0.005)
MD-257kGy-S3	387.5 (10432)	406.7 (12111)	19.5 (12.7)	6.03 (0.88)	9.9 (2.7)	17.0 (5.8)	15.48 (3.54)	142 (1247)	0.493 (0.006)
MD-257kGy-I	399.7 (8965)	428.8 (11226)	19.8 (12.7)	5.32 (1.12)	9.7 (2.5)	17.5 (8.1)	15.06 (2.87)	176 (2723)	0.427 (0.006)
MD-257kGy-S	386.0 (9739)	406.1 (11455)	19.7 (12.0)	5.85 (1.26)	9.9 (2.6)	16.9 (5.5)	15.45 (3.17)	150 (1639)	0.470 (0.006)

Statistical analysis was performed using Gnumeric software. Because normality of these new distributions could not be guaranteed using normality algorithms and variances could differ slightly, irradiated and control specimens data points were compared using the Welch's t-test (mean comparison assuming normal distributed variables but sufficiently robust to deal with non-normal samples if there are enough data points) and Wilcoxon-Mann-Whitney test (median comparison without normality assumption) as a verification both at a confidence level of 5%. There is no significant difference concerning Young's moduli in agreement with the tables. After a total irradiated dose of 257 kGy, there is a significant increase of the creep modulus C of about 17% and a significant decrease of indentation characteristic time τ of about 9% comparing data points obtained from the method herein presented. Box plots summarizing the results are presented in Fig. 12. These proportions are similar to the ones computed from

hierarchical or 3D-microscope analysis outputs but may not be statistically different in the latter cases, especially when data points are identified using 3D-microscope only. Creep modulus increase is correlated with a slight indentation hardness increase of about 6% which is significant for data points obtained using the coupled method. Consequently, h_{max} slightly decreases while n_{IT} slightly increases with irradiations. The indentation energy W_t remains unchanged proving that only slight changes are occurring.

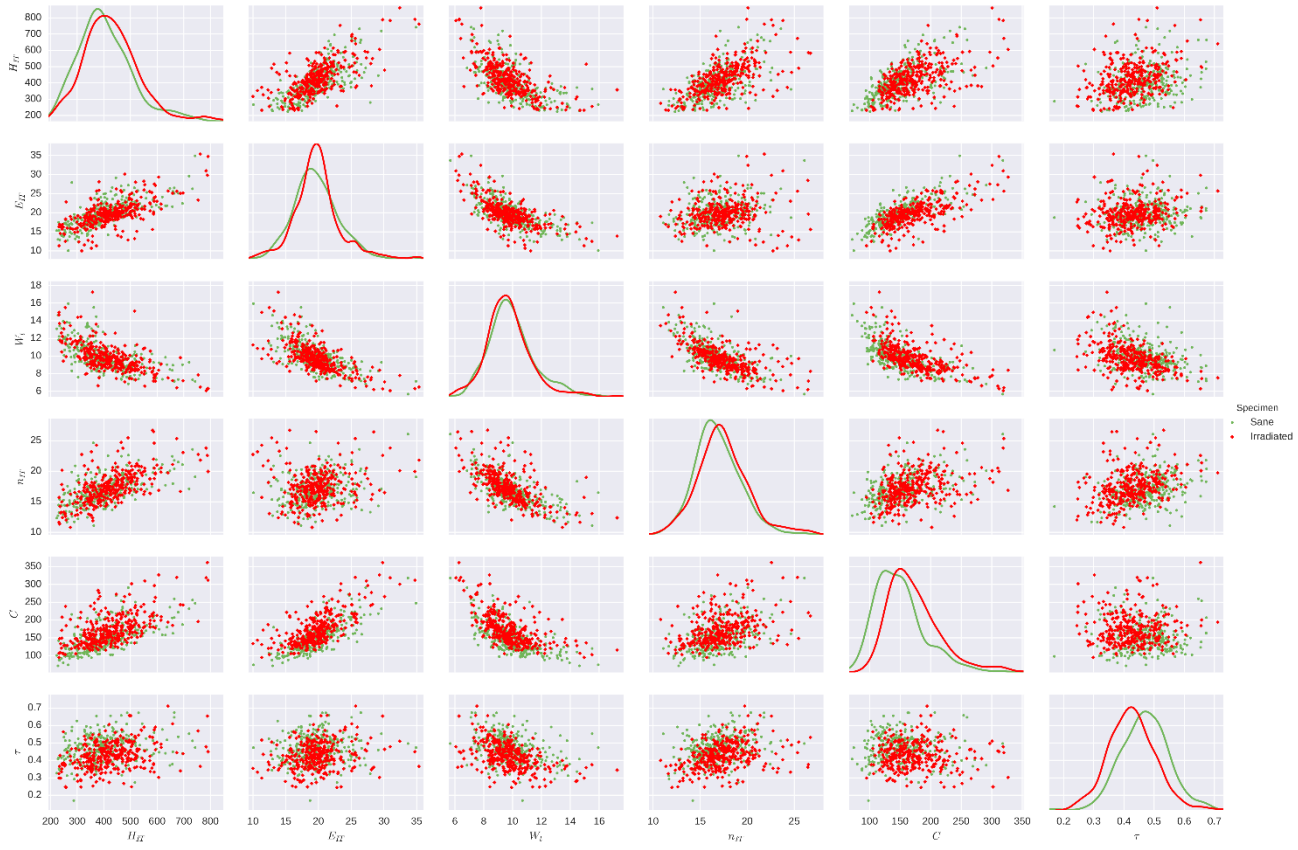

Fig. 11. Scatter plot of indentation data points attributed to the cement paste by coupling data deconvolution and image analysis for irradiated and control specimens (H_{IT} is expressed in MPa, E_{IT} and C in GPa, n_{IT} in %, W_t in µJ and τ in s).

473

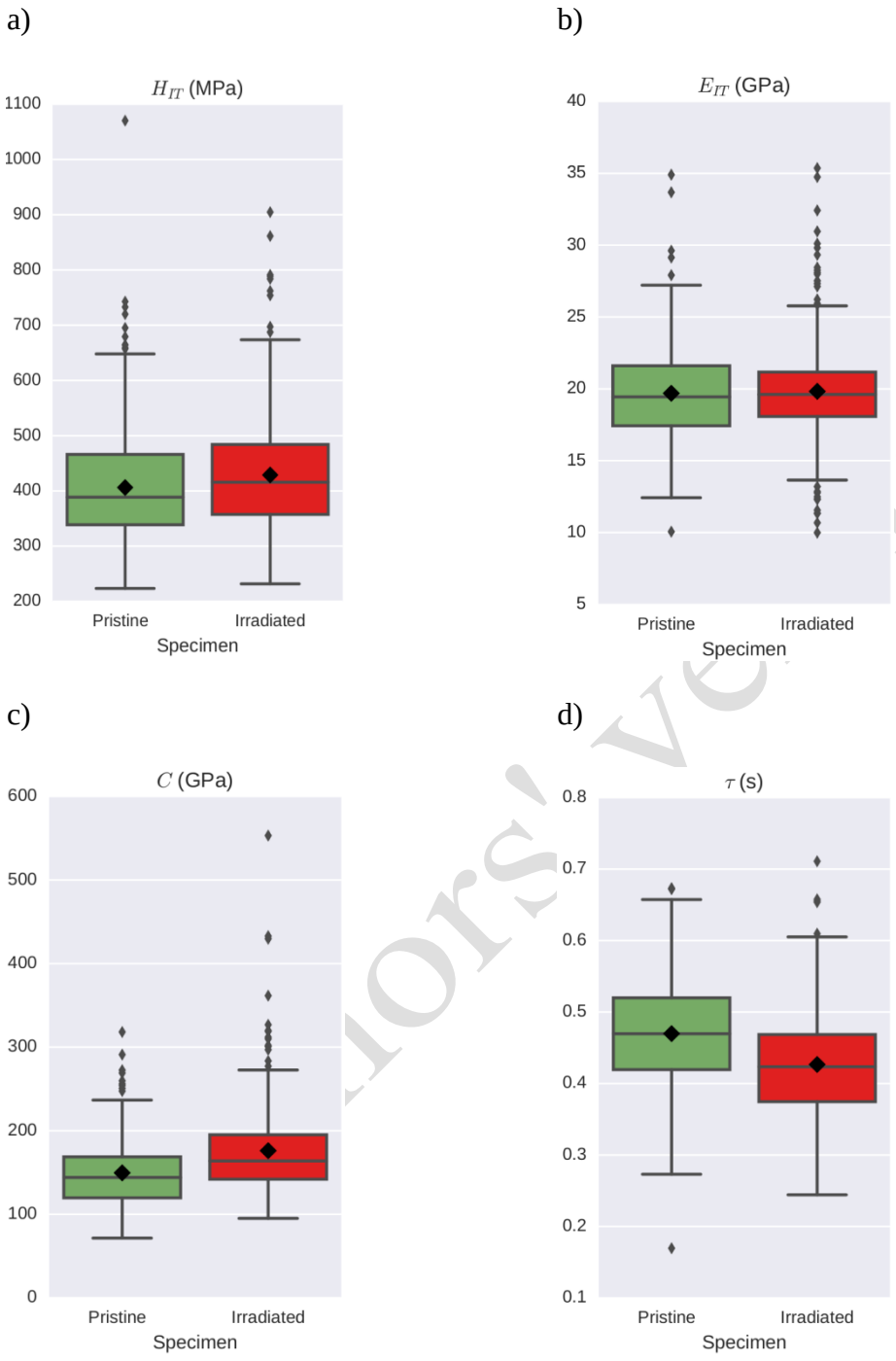

474 **Fig. 12.** Box plots of indentation data points attributed to the cement paste by coupling
475 data deconvolution and image analysis for irradiated and pristine specimens: a) H_{IT}, b)
476 E_{IT}, c) C and d) τ, Center horizontal line of the box represents the median value while
477 thick diamond stands for the mean value.

478

From our knowledge, these creep results are the first microindentation results concerning irradiated concrete specimens. Therefore, it could be interesting to make a comparison with the only macroscopic creep results under γ-irradiation reported a long time ago [39] and illustrated as markers in Fig. 13. The experimental macroscopic specific creep function was first fitted using a classic 3-parameters logarithmic law:

$$J_u(t) - \frac{1}{E_0} = \frac{\ln(t/\tau + 1)}{C} \quad (11)$$

This first fit led to an increase of the creep modulus of 74% (132 GPa for irradiated sample and 76 GPa for control sample) and a decrease of τ of around 49 % (47 d vs 24d). Tough the raw increases are dramatic and somehow affected by the lack of experimental values compared to the number of parameters, this trend qualitatively agrees with the microindentation results. In order to obtain more realistic creep modulus variations, it has been decided to fit the experimental data using a two parameters law written as:

$$J_u(t) - \frac{1}{E_0} = \frac{\ln(t/cste + 1)}{C} \quad (11)$$

Using a characteristic time cste of 25 d (same order of magnitude as the characteristic time using a 3-parameters fit. but still a relatively small value regarding the dose (around 70 kGy) at this time), this type of law correctly describe the creep behavior for times greater than τ. As illustrated in Fig. 13, the fit is acceptable for times greater than approximately 40 d. When applied on the regression curves proposed by McDowall, this fit leads to a more reasonable creep modulus increase of 53% after a total dose 820kGy in approximately 300 d (141 GPa for the irradiated specimen and 92 GPa for the control specimen). This increase is around three times greater than the increase measured by indentation after a total dose of 257 kGy.

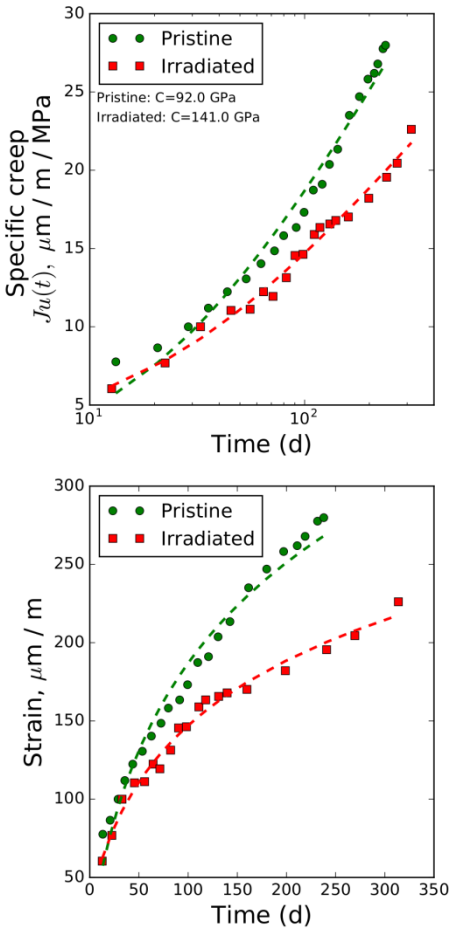

Fig. 13. Comparison between experimental creep results from [39] (markers) and a 2-parameters logarithmic fit (dashed line).

Therefore, in order to compare creep modulus' increase at similar total doses, we performed 2-parameters fitting up to increasing doses with the assumption that irradiation gradually affects cementitious materials. For this purpose, we approximated the initial fit of the evolution of strain proposed by McDowall in order to feed the algorithm with continuous data. Then logarithmic 2-parameters fitting was realized between dose segments of growing sizes beginning by a first segment of [0 kGy, 20 kGy] and gradually increasing the size of the segment by 0.5 kGy. The general trend of the optimization problem for the ratio of the creep modulus evolution assessment, depending on time t and dose d, is summarized by eq. 12 where J' and J are the specific

creep function of the irradiated and control specimens. The resulting evolution of the ratio between the creep moduli of irradiated concrete specimen and control specimen over the total dose is illustrated in Fig. 14.

$$\frac{C_{Irr}(d)}{C_{sane}} = \frac{\min_{C.\tau=25d} \int_0^d J'_{exp}(t.d) - J'_{num}(t.d)}{\min_{C.\tau=25d} \int_0^d J_{exp}(t) - J_{num}(t)} \quad (12)$$

Because the effect of radiations is supposedly small at low doses, creep moduli ratio is close to 1 for small segments and. because the effect of radiation increases with time the ratio gradually increases. It is difficult to say whether the quick increase of the ratio before 50-60 kGy is representative of the concrete behavior or if the fit reliability is affected by the logarithmic function selected (irradiation times are close to the creep characteristic time at low dosage). However, one may observe the ratio exhibits a quasi-linear increase after 180 kGy (doses at which time ≥ 3×creep characteristic time). A linear regression with a correlation coefficient of 0.994 is proposed after 180 kGy. From this regression, it can be stated that the increase rate is of 5×10^{-2}% / kGy, which leads, considering and initial creep modulus of around 100 GPa, to a rate of 50 GPa/MGy. For a dose of 257 kGy, the increase of the creep modulus from this method is around 20% which is in good agreement with the increase calculated from the microindentation experiment.

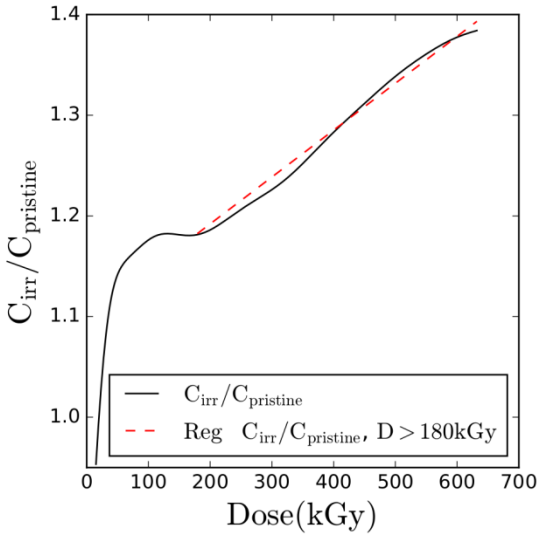

Fig. 14. Evolution of the ration between creep moduli calculated for irradiated and control concrete specimens from [39] relatively to the final dose considered for a 2-parameters fitting logarithmic law.

4. Conclusion and perspectives

In this study, the potential of coupling indentation and optical microscopy for heterogenous materials characterization has been demonstrated. A novel method has been introduced to reduce the variability of the micromechanical properties associated to an indented phase. This method relies on the comparison of the nature of indents numerically predicted by statistical indentation data deconvolution and by 3D-optical microscope image analysis. This method robustly counteracts the uncertainty of numerical clustering methods by introducing optical information. In our study, the data points cluster of interest generated by the method associated with cement paste likely exhibits a normal distribution and a systematic reduced variance compared to each of the technique alone. This herein described method could be applied to a wide range of materials and studies.

The proposed method was successfully applied to the assessment of micro-mechanical properties of γ-irradiated mortar specimens. The method led to the identification of the

cement paste elasto-plastic parameters affected by irradiation at relatively low cumulated dose of 257 kGy. It has been found out that creep modulus C significantly increases by around 17% and indentation characteristic time γ significantly decreases by around 9% after irradiation. The creep modulus increase is correlated with a slight increase of the indentation hardness H_{IT} and of the proportion of the elastic response relatively to the total energy n_{IT}. On the other hand, Young's modulus of irradiated specimens does not significantly differ from the one of control specimens.

These micro-mechanical observations agree with the only macroscopic uniaxial compressive creep measurements under γ-irradiation published to our knowledge [39]. Using a logarithmic dose-dependant fit of the specific creep function proposed in this study, it can be calculated that the creep modulus increases and the creep characteristic time decreases leading to less creep of the irradiated samples. Then a reverse analysis was proposed to quantify the evolution of the irradiated vs pristine creep moduli ratio with the time increasing γ-dose. Although supplementary similar experiments should be carried out at both microscale and macroscale with various dose rates, the creep modulus appears to linearly increase with the γ-dose for doses between 180 and 700 kGy.

Acknowledgments

The authors gratefully acknowledge the financial support provided for this study by Tractebel Engineering. Special thanks are due to Xavier Bourbon (ANDRA) for instructive discussions. This work has been supported in part by a grant from the French National Agency for Research called "Investissements d''Avenir". Equipex ArronaxPlus n°ANR-11-EQPX-0004.

References

[1] P. Trtik and P. J. M. Bartos. Micromechanical properties of cementitious composites. *Materials and Structures*, 32(5):388–393, 1999.

[2] P. Acker. Micromechanical analysis of creep and shrinkage mechanisms. In *Creep, shrinkage and durability mechanics of concrete and other quasi-brittle materials. (Proceedings of ConCreep6)*, 2001.

[3] K. Velez, S. Maximilien, D. Damidot, G. Fantozzi, and F. Sorrentino. Determination by nanoindentation of elastic modulus and hardness of pure constituents of portland cement clinker. *Cement and Concrete Research*, 31(4):555 – 561, 2001.

[4] G. Constantinides, F.-J. Ulm, and K. Van Vliet. On the use of nanoindentation for cementitious materials. *Materials and Structures*, 36(3):191–196, 2003.

[5] G. Constantinides and F.-J. Ulm. The effect of two types of c-s-h on the elasticity of cement-based materials: Results from nanoindentation and micromechanical modeling. *Cement and Concrete Research*, 34:67–80, 2004.

[6] J. J. Chen, L. Sorelli, M. Vandamme, F.-J. Ulm, and G. Chanvillard. A coupled nanoindentation/sem-eds study on low water/cement ratio portland cement paste: Evidence for c-s-h/ca(oh)2 nanocomposites. *Journal of the American Ceramic Society*, 93(5):1484–1493, 2010.

[7] M. Vandamme and F.-J. Ulm. Nanoindentation investigation of creep properties of calcium silicate hydrates. *Cement and Concrete Research*, 52:38 – 52, 2013.

[8] W.C. Oliver and G.M. Pharr. An improved technique for determining hardness and elastic modulus using load and displacement sensing indentation experiments. *Journal of Materials Research*, 7:1564–1583, 1992.

[9] F.-J. Ulm, M. Vandamme, C. Bobko, J.A. Ortega, K. Tai, and C Ortiz. Statistical indentation techniques for hydrated nanocomposites: Concrete, bone, and shale. *Journal of the American Ceramic Society*, 90:2677–2692, 2007.

[10] L. Sorelli, G. Constantinides, F.-J. Ulm, and F. Toutlemonde. The nano-mechanical signature of ultra high performance concrete by statistical nanoindentation techniques. *Cement and Concrete Research*, 38(12):1447 – 1456, 2008.

[11] C. Hu, Y. Gao, Y. Zhang, and Z. Li. Statistical nanoindentation technique in application to hardened cement pastes: Influences of material microstructure and analysis method. *Construction and Building Materials*, 113:306 – 316, 2016.

[12] P. Trtik, B. Münch, and P. Lura. A critical examination of statistical nanoindentation on model materials and hardened cement pastes based on virtual experiments. *Cement and Concrete Composites*, 31(10):705 – 714, 2009.

[13] F.-J. Ulm, M. Vandamme, H. M. Jennings, J. Vanzo, M. Bentivegna, K. J. Krakowiak, G. Constantinides, C. P. Bobko, and K. J. Van Vliet. Does microstructure matter for statistical nanoindentation techniques? *Cement and Concrete Composites*, 32(1):92 – 99, 2010.

[14] D. Davydov, M. Jirásek, and L. Kopecký. Critical aspects of nano-indentation technique in application to hardened cement paste. *Cement and Concrete Research*, 41(1):20 – 29, 2011.

[15] P. Lura, P. Trtik, and B. Münch. Validity of recent approaches for statistical nanoindentation of cement pastes. *Cement and Concrete Composites*, 33(4):457 – 465, 2011.

[16] P. Mondal, S. P. Shah, and L. Marks. A reliable technique to determine the local mechanical properties at the nanoscale for cementitious materials. *Cement and Concrete Research*, 37(10):1440 – 1444, 2007.

[17] J. J. Hughes and P. Trtik. Micro-mechanical properties of cement paste measured by depth-sensing nanoindentation: a preliminary correlation of physical properties with phase type. *Materials Characterization*, 53:223 – 231, 2004. EMABM 2003: 9th Euroseminar on Microscopy Applied to Building Materials.

[18] C. Hu and Z. Li. Micromechanical investigation of portland cement paste. *Construction and Building Materials*, 71:44 – 52, 2014.

[19] W. Zhu, J. J. Hughes, N. Bicanic, and Chris J. Pearce. Nanoindentation mapping of mechanical properties of cement paste and natural rocks. *Materials Characterization*, 58:1189 – 1198, 2007. 10th Euroseminar on Microscopy Applied to Building Materials (EMABM).

[20] S. Zhao and W. Sun. Nano-mechanical behavior of a green ultra-high performance concrete. *Construction and Building Materials*, 63:150 – 160, 2014.

[21] M. Vandamme, F.-J. Ulm, and P. Fonollosa. Nanogranular packing of C-S-H at substochiometric conditions. *Cement and Concrete Research*, 40(1):14 – 26, 2010.

[22] A. B. Nichols and D. A. Lange. 3d surface image analysis for fracture modeling of cement-based materials. *Cement and Concrete Research*, 36(6):1098 – 1107, 2006.

[23] T. Ficker, D. Martisek, and H. M. Jennings. Roughness of fracture surfaces and compressive strength of hydrated cement pastes. *Çement and Concrete Research*, 40(6):947 – 955, 2010.

[24] B. Hilloulin, J.-B. Legland, E. Lys, O. Abraham, A. Loukili, F. Grondin, O. Durand, and V. Tournat. Monitoring of autogenous crack healing in cementitious materials by the nonlinear modulation of ultrasonic coda waves, 3d microscopy and x-ray microtomography. *Construction and Building Materials*, 123:143 – 152, 2016.

[25] Q. Zhang, R. Le Roy, M. Vandamme, and B. Zuber. Long-term creep properties of cementitious materials: Comparing microindentation testing with macroscopic uniaxial compressive testing. *Cement and Concrete Research*, 58:89 – 98, 2014.

[26] M. Irfan-ul-Hassan, B. Pichler, R. Reihsner, and Ch. Hellmich. Elastic and creep properties of young cement paste, as determined from hourly repeated minute-long quasi-static tests. *Cement and Concrete Research*, 82:36 – 49, 2016.

[27] D.-T. Nguyen, R. Alizadeh, J. J. Beaudoin, P. Pourbeik, and L. Raki. Microindentation creep of monophasic calcium-silicate-hydrates. *Cement and Concrete Composites*, 48:118 – 126, 2014.

[28] J. Frech-Baronet, L. Sorelli, and J.-P. Charron. New evidences on the effect of the internal relative humidity on the creep and relaxation behaviour of a cement paste by micro-indentation techniques. *Cement and Concrete Research*, 91:39 – 51, 2017.

[29] K.G. Field, I. Remec, and Y. Le Pape. Radiation effects in concrete for nuclear power plants - part i: Quantification of radiation exposure and radiation effects. *Nuclear Engineering and Design*, 282:126 – 143, 2015.

[30] Y. Le Pape, K.G. Field, and I. Remec. Radiation effects in concrete for nuclear power plants, part ii: Perspective from micromechanical modeling. *Nuclear Engineering and Design*, 282:144 – 157, 2015.

[31] A. Giorla, M. Vaitová, Y. Le Pape, and P. Štemberk. Meso-scale modeling of irradiated concrete in test reactor. *Nuclear Engineering and Design*, 295:59 – 73, 2015.

[32] H. K. Hilsdorf, J. Kropp, and H. J. Koch. The effects of nuclear radiation on the mechanical properties of concrete. Technical report, ACI SP-55, 1978.

[33] ANDRA. Dossier 2005 argile, architecture and management of a geological repository. Technical report, ANDRA, 2005.

671 [34] P. Soo and L. M. Milian. The effect of gamma radiation on the strength of
672 portland cement mortars. *Journal of Materials Science Letters*, 20(14):1345–1348,
673 2001.
674 [35] F. Vodák, K. Trtík, V. Sopko, O. Kapicková, and P. Demo. Effect of γ -
675 irradiation on strength of concrete for nuclear-safety structures. *Cement and Concrete*
676 *Research*, 35(7):1447 – 1451, 2005.
677 [36] O. Kontani, Y. Ichikawa, A. Ishizawa, M. Takizawa, and O. Sato. Irradiation
678 effects on concrete structures. In *International Symposium on the Ageing Management*
679 *& Maintenance of Nuclear Power Plants*, 2010.
680 [37] O. Kontani, S. Sawada, I. Maruyama, M. Takizawa, and O. Sato. Evaluation of
681 irradiation effects on concrete structure - gamma - ray irradiation test on cement paste.
682 In *Proceedings of the ASME 2013 Power Conference (POWER2013), July 29-August 1,*
683 *2013, Boston, Massachusetts, USA*, 2013.
684 [38] A. Lowinska-Kluge and P. Piszora. Effect of gamma irradiation on cement
685 composites observed with XRD and SEM methods in the range of radiation dose 0 -
686 1409 MGy. *Acta Physica Polonica, A*, 114:399 – 411, 2008.
687 [39] D. McDowall. The effects of gamma radiation on the creep properties of
688 concrete. In *Proceedings of the Information Exchange Meeting on 'Results of Concrete*
689 *Irradiation Programs', EUR 4751 f-e, Commission des Communautés Européennes,*
690 *Brussels, Belgium*, 1971.
691 [40] R.L. Grossman, C. Kamath, P. Kegelmeyer, V. Kumar, and R. Namburu. *Data*
692 *Mining for Scientific and Engineering Applications*. Springer US, 2001.
693 [41] Krishna Rajan. Materials informatics. *Materials Today*, 8(10):38 – 45, 2005.
694 [42] J.H. Koo. *Polymer Nanocomposites: Processing, Characterization, and*
695 *Applications*. McGraw-Hill, New York, 2006.

696 [43] S. K. Barai. Data mining applications in transportation engineering. *Transport*,
697 18(5):216–223, 2003.
698 [44] F. Vodák, V. Vydra, K. Trtík, and O. Kapicckovᡠ. Effect of gamma irradiation
699 on properties of hardened cement paste. *Materials and Structures*, 44:101 – 107, 2011.
700 [45] M. Miller, C. Bobko, M. Vandamme, and F.-J. Ulm. Surface roughness criteria
701 for cement paste nanoindentation. *Cement and Concrete Research*, 38(4):467 – 476,
702 2008.
703
704